Journal of Materials Chemistry C

Accepted Manuscript

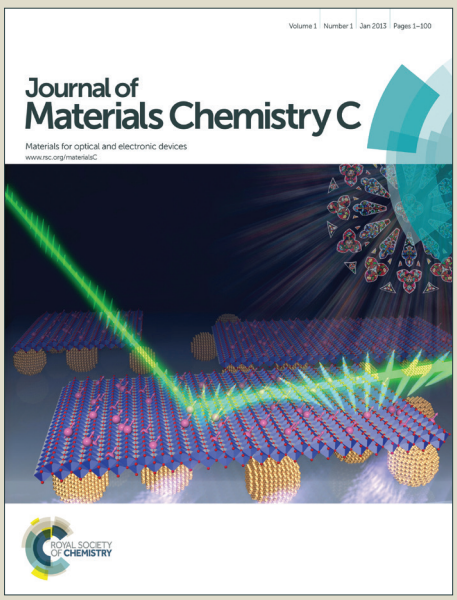

ROYAL SOCIETY OF CHEMISTRY

www.rsc.org/materialsC

Journal Name

ARTICLE TYPE

Cite this: DOI: 10.1039/xxxxxxxxxx

Fine tuning of thermoelectric performance in phase-separated half-Heusler compounds

Elisabeth Rausch,[a,b] Benjamin Balke,*[a] Jana Marie Stahlhofen,[a] Siham Ouardi,[b] Ulrich Burkhardt[b] and Claudia Felser[b]

Received Date
Accepted Date

DOI: 10.1039/xxxxxxxxxx

www.rsc.org/journalname

Two succesful recipes to enhance the thermoelectric performance, namely carrier concentration optimization and reduction of thermal conductivity, have been combined and applied to the *p*-type (Ti/Zr/Hf)$CoSb_{1-x}Sn_x$ system. An intrinsic micrometer-scale phase separation increases the phonon scattering and reduces the lattice thermal conductivity. A substitution of 15% Sb by Sn optimizes the electronic properties. Starting from this, further improvement of the thermoelectric properties has been achieved by a fine tuning of the Ti to Hf ratio. The microstructuring of the samples was studied in detail with high-resolution synchrotron powder X-ray diffraction and element mapping electron microscopy. Linking the structural with the thermoelectric properties, a record thermoelectric figure of merit for *p*-type half-Heusler compounds of $ZT \approx 1.2$ at 710 °C in $Ti_{0.25}Hf_{0.75}CoSb_{0.85}Sn_{0.15}$ was achieved. The phase separation approach can form a significant alternative to nanostructuring processing, saving time, energy consumption and increasing the thermoelectric efficiency.

1 Introduction

Intermetallic half-Heusler compounds with the structural formula *XYZ* crystallizing in the cubic structure $F\bar{4}3m$ have recently gained attention as promising materials for moderate-temperature thermoelectric (TE) applications such as industrial and automotive waste heat recovery.[1] An industrial upscaling of the synthesis of both *p*-type and *n*-type materials has been realized, and such thermoelectric modules have been tested for their long-term stability and reproducibility.[2] However, their performance still needs to be improved by adoption of the optimal material composition to reach the cost efficiency of industrial applications.

A great advantage of half-Heusler compounds is the possibility to substitute each of the three occupied fcc sublattices individually. The number of charge carriers can be tuned by substitution of the *Z*-position element by another main-group element. Simultaneously, disorder can be introduced by substitution on the *X*- and *Y*-position elements resulting in mass fluctuations, which can decrease the thermal conductivity κ.[3] In general, half-Heusler compounds exhibit high power factors in the range of 2–6$\times 10^{-3}$Wm^{-1}K^{-1}.[1,3–5] Thus, the main obstacle to further improving their TE performance is their relatively high thermal conductivity. Recently, the concept of an intrinsic phase separation has become a focus of research. In particular, the *n*-type (Ti/Zr/Hf)NiSn system has been investigated in this regard[6–11] leading to several patent applications.[12–15] Very recently, the stability of the submicrostructuring and thermoelectric properties under thermal cycling conditions was proven.[16]

In contrast, state-of-the-art *p*-type half-Heusler materials rely on a nanostructuring approach involving ball milling followed by a rapid consolidation method which is a very time and energy consuming synthesis route.[17,18] It was recently demonstrated that the concept of phase separation can also be applied to the *p*-type material system (Ti/Zr/Hf)$CoSb_{0.8}Sn_{0.2}$. An effective reduction of the thermal conductivity is achieved by the intrinsic microstructuring, for which the partial substitution of Ti with Hf is mandatory.[19]

Thus far, the best *p*-type half-Heusler materials are based on a substitution of 20% Sn on the Sb-position in the (Ti/Zr/Hf)CoSb material system.[17,20–22] An additional adjustment of the carrier concentration further enhances the power factor. Optimum is a substitution level of 15% Sn on the Sb-position.[23] This work combines both concepts in the investigation of the $Ti_{1-x}Hf_xCoSb_{0.85}Sn_{0.15}$ system. A fine-tuning of the TE performance via the adjustment of the Ti to Hf ratio is possible and the resulting TE properties correlate to the results of the structural investigations.

[a] *Institute for Inorganic and Analytical Chemistry, Johannes Gutenberg-University, D-55099 Mainz, Germany. Fax: +49 6131 39 26267; Tel: +49 6131 39-26902; E-mail: balke@uni-mainz.de*
[b] *Max Planck Institute for Chemical Physics of Solids, D-01187 Dresden, Germany.*

2 Experimental details

Ingots of ca. 15 g were prepared by arc melting of the stoichiometric amounts of the elements. For homogenization, each sample was crushed and remelted several times. At each step, the weight loss due to the high vapor pressure of Sb was compensated by addition of Sb until no evaporation was observed during the melting process. The samples were annealed in evacuated quartz tubes at 900°C for seven days and subsequently quenched in ice water. For a detailed study upon fabrication process and reproducibility of phase separated half-Heusler compounds see reference[23]. The crystal structure was analyzed by X-ray powder diffraction (XPD) with Cu$K_{\alpha 1}$ radiation at room temperature using an image-plate Huber G670 Guinier camera equipped with a Ge(111) monochromator operating in the range $10^\circ \leq 2\theta \leq 100^\circ$. To investigate the phase separation in detail all samples were analyzed using high-resolution X-ray powder diffraction with synchrotron radiation with $\lambda = 1.65307$ Å. The experiments were performed at the XPD beamline at the bending magnet D10 at the Brazilian Synchrotron Light Laboratory (LNLS). For details regarding the characteristics of the beamline see, e.g., reference[24].

Microstructures characterization were performed on metallographically prepared cross-section of approximetaly 4×1 mm^2. The phase distribution was documented by optical (Zeiss, Axioplan) and scanning electron microscopy (SEM, Philips XL30 with LaB6 cathode). The semi-quantitative determination of the chemical composition and the recording of the qualitative element distribution were realized by using the element specific X-ray intensities measured with an energy dispersive detector (Bruker, XFlash SDD 30 mm) that was attached to the SEM. An acceleration voltage of 25 kV and the spot mode were used for the determination of the chemical compositions of the phases. The PB-Phi(Rho-z) matrix correction model was applied for calculation of the composition (Bruker, Quantax 400 software package Ver. 1.9.4). The composition of the half-Heusler phases, as indicated in Table 1, was determined by chosing several spots of the same phase and averaging the composition. The standard deviation for each element was $< 4\%$, which is within the error range of the method. Hypermaps with enhanced count rates were recorded over an interval of 60 min, and the element-distribution images were extracted from the deconvoluted intensities of the X-ray lines. In case of Hf, the M_α line instead of the L_α line was selected to represent the Hf distribution due to the better spatial resolution obtained in the former case. For all other elements, the same X-ray lines were used for the quantification and the element distribution images.

To investigate the thermoelectric properties at high temperature, the ingots were cut into discs and bars. The Seebeck coefficients S and electrical conductivity σ were determined simultaneously using an LSR-3 (Linseis). The thermal conductivity κ was calculated using the relation $\kappa = C_p \alpha \rho$, where C_p denotes the specific heat capacity, α the thermal diffusivity, and ρ the density. The values α were measured by means of the laser flash method using the Netzsch LFA 457 instrument. The density ρ was calculated from the mass and volume of the cut bars. The heat capacities were estimated by means of the Dulong–Petit law. The uncertainties were 3% for the electrical conductivity and thermal diffusivity and 5% for the Seebeck coefficient, thereby leading to an 11% uncertainty in the Figure of merit $ZT = \frac{S^2\sigma}{\kappa}T$ by propagation of error. We measured the samples numereous times while they were heated up to 700°C and cooled, and verified that there was no degradation in the various sample properties.

The transport properties at low temperatures were determined by a Physical Properties measuerment system (PPMS, Quantum design) using the Thermal Transport Option (TTO) for thermoelectric properties and the AC Transport Option (AC-T) for Five-Wire Hall Coefficient R_H and resistivity ρ measurements. From these values the carrier concentration $n_H = -\frac{1}{R_H e}$ and mobility $\mu_H = \frac{1}{\rho n_H e}$ with e elementary charge, were determined.

3 Results and discussion

3.1 Microstructure investigations

The investigations of the samples by X-ray powder diffraction (XPD), scanning electron microscopy (SEM), and energy-dispersive X-ray (EDX) spectroscopy revealed that samples containing Ti and Hf undergo an intrinsic phase separation into two half-Heusler phases. The composition of the matrix (phase I) and the second half-Heusler phase (phase II) as determined by EDX spectroscopy are indicated in Table 1.

In general, we note that the matrix is rich in Hf and Sb whereas the second phase is rich in Ti and Sn when compared with the nominal composition. Moreover, this second phase has a slight excess of Co. We assume that the Co atoms occupy the vacant tetrahedral holes in the structure that is similar to the $L2_1$ Heusler compound Co_2TiSn.[25] Our assumption is supported by a recent report on the in-situ growth of Heusler quantum dots in the half-Heusler $Ti_{0.5}Hf_{0.5}CoSb_{0.8}Sn_{0.2}$ matrix.[26] In addition, very small amounts of the pure elements Ti, Sn or Hf or a binary Ti_ySn_z were detected. These results agree well with our previous investigations of the phase separation in the (Ti/Zr/Hf)$CoSb_{0.8}Sn_{0.2}$ system.[19]

The typical microstructure of the samples is displayed in the backscattered electron images (BSE) in Figures 1(a)-(f). The amount and shape of the second half-Heusler phase depends on the ratio of Ti to Hf. Samples with $0.75 \geq x \geq 0.25$ show a fine network of the second phase within the matrix. The most distinctive formation is observed for the composition with $x = 0.25$. Upon decreasing the amount of Ti further ($x = 0.85$), the amount of the second half-Heusler phase becomes too less to form an interconnecting network. The element-specific EDX mappings (see Figure 2 for the sample with x = 0.25) confirm that the second half-Heusler phase is rich in Ti and Sn and exhibits a slight excess of Co. The images of the distributions of these three elements all appear similar, whereas the element-specific mappings for Hf and Sb appear as "negatives" of the images of the other three elements.

X-ray diffraction patterns of the substitution series $Ti_{1-x}Hf_xCoSb_{0.85}Sn_{0.15}$ using a Cu$K_{\alpha 1}$ lab source confirmed the presence of half-Heusler structure $C1_b$ in all compounds

Table 1 Composition of the matrix (I) and second half-Heusler phases (II) of the samples $Ti_{1-x}Hf_xCoSb_{0.85}Sn_{0.15}$ as determined by EDX spectroscopy. Experimental density ρ, carrier concentration n_H, and Hall mobility μ_H at 300 K.

Nominal composition	Phase	EDX	ρ / g×cm^{-3}	n_H / 10^{21} cm^{-3}	μ_H / 10^2cm^{2}V^{-1}s^{-1}
$TiCoSb_{0.85}Sn_{0.15}$	I	$Ti_{1.07}Co_{0.98}Sb_{0.91}Sn_{0.05}$	7.312	0.780	1.734
	II	$Ti_{0.97}Co_{1.18}Sb_{0.28}Sn_{0.57}$			
$Ti_{0.75}Hf_{0.25}CoSb_{0.85}Sn_{0.15}$	I	$Ti_{0.79}Hf_{0.25}Co_{0.97}Sb_{0.94}Sn_{0.04}$	8.161	1.093	2.325
	II	$Ti_{0.95}Hf_{0.09}Co_{1.06}Sb_{0.36}Sn_{0.55}$			
$Ti_{0.5}Hf_{0.5}CoSb_{0.85}Sn_{0.15}$	I	$Ti_{0.44}Hf_{0.55}Co_{1.02}Sb_{0.94}Sn_{0.05}$	8.983	0.995	2.794
	II	$Ti_{0.80}Hf_{0.21}Co_{1.07}Sb_{0.33}Sn_{0.59}$			
$Ti_{0.25}Hf_{0.75}CoSb_{0.85}Sn_{0.15}$	I	$Ti_{0.17}Hf_{0.79}Co_{1.01}Sb_{0.98}Sn_{0.06}$	9.849	0.916	3.492
	II	$Ti_{0.60}Hf_{0.38}Co_{1.09}Sb_{0.27}Sn_{0.66}$			
$Ti_{0.15}Hf_{0.85}CoSb_{0.85}Sn_{0.15}$	I	$Ti_{0.10}Hf_{0.86}Co_{1.03}Sb_{0.94}Sn_{0.07}$	9.705	1.237	4.282
	II	$Ti_{0.47}Hf_{0.48}Co_{1.11}Sb_{0.29}Sn_{0.65}$			
$HfCoSb_{0.85}Sn_{0.15}$	I	$Hf_{0.93}Co_{1.02}Sb_{0.97}Sn_{0.08}$	10.581	1.480	4.965
	II	$Hf_{0.86}Co_{1.19}Sb_{0.26}Sn_{0.69}$			

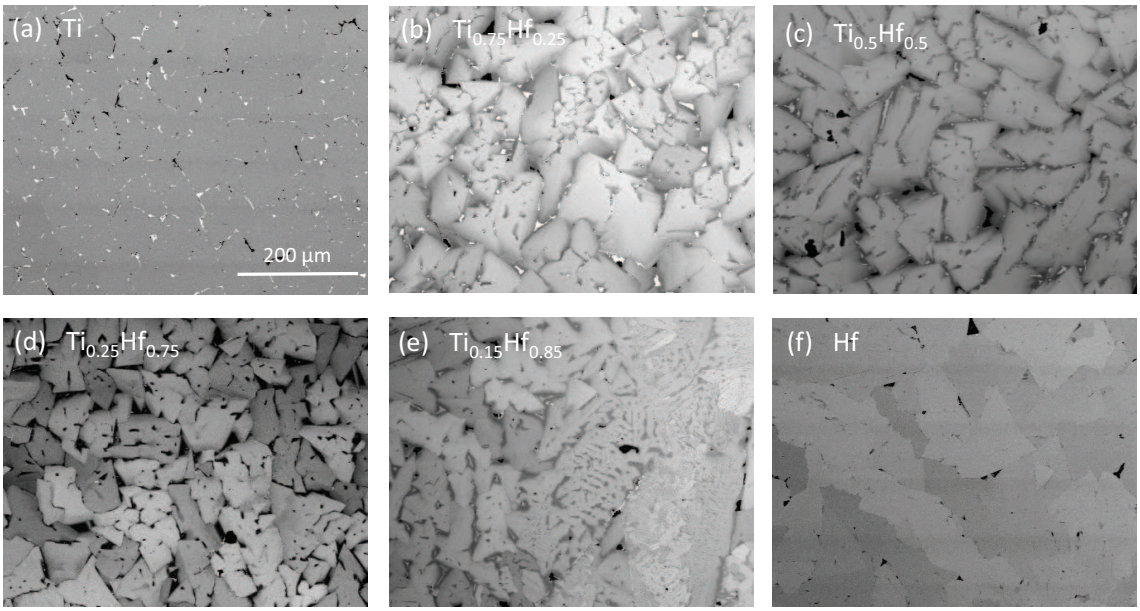

Fig. 1 Backscattered electron images of $Ti_{1-x}Hf_xCoSb_{0.85}Sn_{0.15}$ with the indicated ratios of Ti to Hf. The matrix (mid-scale grey) is interlaced by a second half-Heusler phase (dark regions), and the bright spots indicate Sn inclusions.

despite the presence of a marginal amount of β-Sn close to the detection limit. Figure 3(a) shows the representative XPD pattern of $HfCoSb_{0.85}Sn_{0.15}$ with the indexed reflections. However, high-resolution XPD with synchrotron radiation revealed the existence of a multiphase state in samples with $0.25 \leq x \leq 0.85$, thus confirming phase separation into different half-Heusler phases, as observed by EDX analysis. Samples with a single element Ti ($x = 0$) or Hf ($x = 1$) exhibited sharp and symmetric Bragg reflections, thereby indicating the presence of only one phase with the $C1_b$ structure. The reflections for a composition of $x = 0.15$ show very little broadening of the peaks. In contrast, the splitting of the main reflection (220) becomes very obvious for samples with $0.25 \leq x \leq 0.75$ (see Figure 3(b)) due to the presence of several half-Heusler phases. For example, the fitting of the powder pattern of $Ti_{0.5}Hf_{0.5}CoSb_{0.85}Sn_{0.15}$ requires at least the presence of five different half-Heusler phases with very similar lattice parameters a (see Figure 3(c)). As an initial assumption, we used the composition of the two half-Heusler phases, that were distinguishable by EDX spectroscopy (see Table 1), and refined the lattice parameters. Subsequently, more phases with the $C1_b$ structure were added to model the shape of the (220) reflection correctly. Since the composition at the phase boundaries is changing gradually, a multiphase state is observed in the high-resolution XPD patterns. Due to the limited lateral and quantititative resolution of the EDX detector, these were not distinguishable by EDX analysis.

3.2 Thermoelectric properties

The thermal conductivity plots of the investigated compounds are displayed in Figure 4. These values are highest for single-phase samples with $x = 0$ and $x = 1$. The thermal conductivity is effectively suppressed by the intrinsic phase separation and depends on the microstructuring of the samples. All samples with a Hf content of $0.25 \leq x \leq 0.75$ exhibit very similar thermal conductivities. The values are nearly temperature-independent, thereby indicating a glass-like behavior. A slightly higher thermal conductivity was observed for samples with $x = 0.85$. To further examine the impact of the substitution level, we calculated the lattice thermal conductivity by applying the Wiedemann–Franz law (see Figure 4(c)). The Lorentz number was estimated with

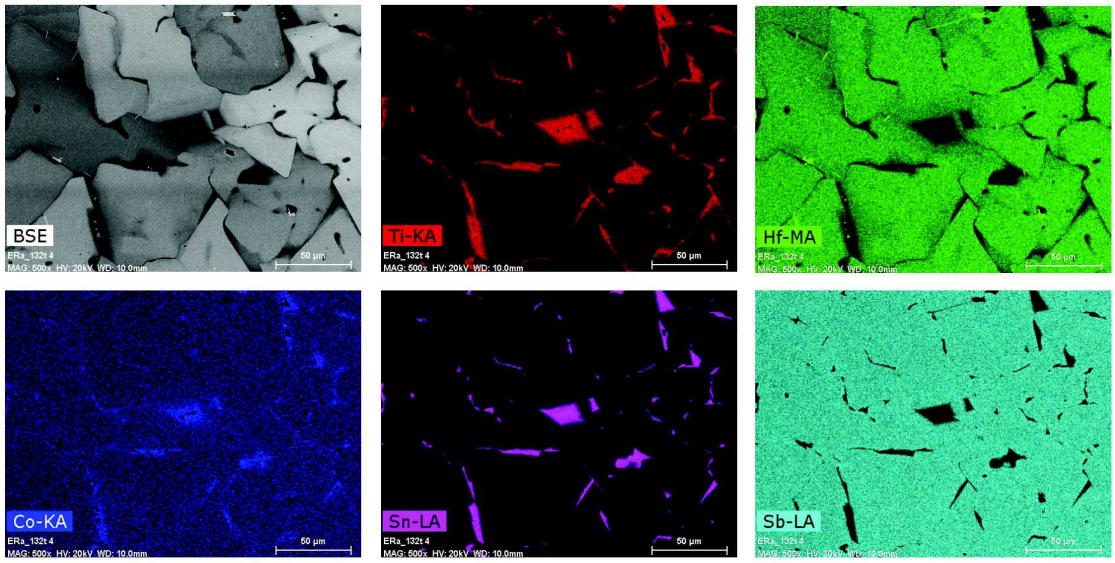

Fig. 2 Element-specific EDX mapping of the sample $Ti_{0.25}Hf_{0.75}CoSb_{0.85}Sn_{0.15}$.

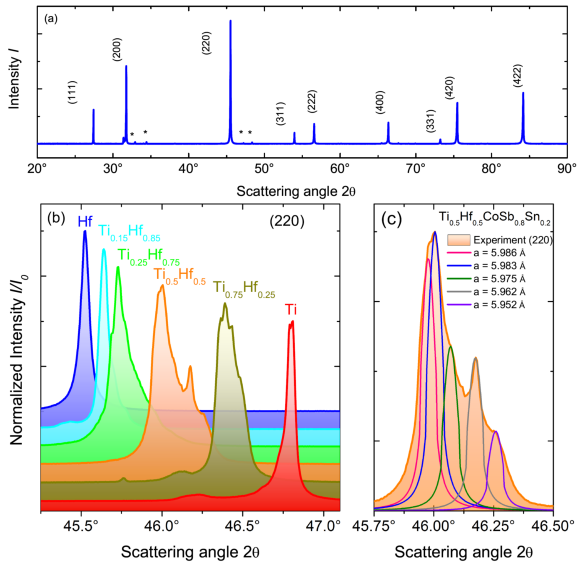

Fig. 3 (a) X-ray powder diffraction pattern (XPD) of $HfCoSb_{0.85}Sn_{0.15}$ obtained using synchrotron radiation (λ =1.65307 Å; * indicates β-Sn). (b) XPD of the main reflection (220) of $Ti_{1-x}Hf_xCoSb_{0.85}Sn_{0.15}$ with the indicated ratios of Ti to Hf, (c) fitting of the (220) reflections for $Ti_{0.5}Hf_{0.5}CoSb_{0.85}Sn_{0.15}$.

$L = 1.5 + exp\left[-\frac{|S|}{116}\right]$.[27] The lowest κ_{lat} values were reached by the samples with $x = 0.25$ (2.01 $Wm^{-1}K^{-1}$ at 980 K), $x = 0.5$ (2.16 $Wm^{-1}K^{-1}$), and $x = 0.75$ (2.05 $Wm^{-1}K^{-1}$). The formation of a interconneting network of second half-Heusler phase within the matrix, leads to an effective reduction of the lattice thermal conductivity. In contrast samples with Hf content of $x = 0.85$ exhibited the highest lattice thermal conductivity among all phase-separated samples (2.30 $Wm^{-1}K^{-1}$ at 980 K).

In this samples the amount of the secondary half-Heusler phase is so small, that it cannot form a interconnecting network through the matrix anymore. This agrees well with the results from the high-resolution XPD. The shape and width of the (220) reflection for $x = 0.85$ is similar to that of the single phase samples in contrast to the splitting of the main reflection for samples with $0.25 \leq x \leq 0.75$. Therefore, phonon scattering is most effective in the sample with $x = 0.75$ corresponding to a reduction of 45% in the lattice thermal conductivity when compared with that of the single-phase $TiCoSb_{0.85}Sn_{0.15}$.

Figure 5(a) shows the temperature dependency of the electrical conductivity σ, for all the samples. All samples exhibit a metallic behavior, i.e., the conductivity decreases with increasing temperature. Upon substitution of Ti with its heavier homologue Hf, σ is enhanced. Due to the interrelation of the Seebeck coefficient with σ, the Seebeck coefficients also shows a decrease upon substitution. The maximum Seebeck coefficient was observed for $TiCoSb_{0.85}Sn_{0.15}$, with a value of 278 μV/K at 780 K. This maximum is shifted to higher temperatures upon substitution of Ti by Hf. Even though the substitution is isoelectronic, it changes the electronic structure and consequently affects the carrier concentration and effective mass of the charge carriers. The carrier concentration n_H and mobilities μ_H at room temperature are listed in table 1. Substitution of Ti by its heavier homologue Hf leads to an increase of n_H as well as of μ_H. Certainly, the impact is small as compared to doping with holes by replacing Sb with Sn, that leads to an increase in n_H with a factor 4 times the substitution level.[23] Regardless, in the cleary phase-separated samples with x = 0.5 and 0.75, n_H as well as μ_H are smaller than one would expect, if one assumes a linear increase with substitution level x. As a consequence the Seebeck coeffiecients are decreased with increasing Hf content, but the phase separation attenuates this effect. In contrast, the electrical conductivity is not affected by the phase separation because the increasing mobility is compensating for the carrier concentration.

The calculation of the power factor $S^2\sigma$ reveals that the optimal electronic properties are obtained for samples with a Hf content

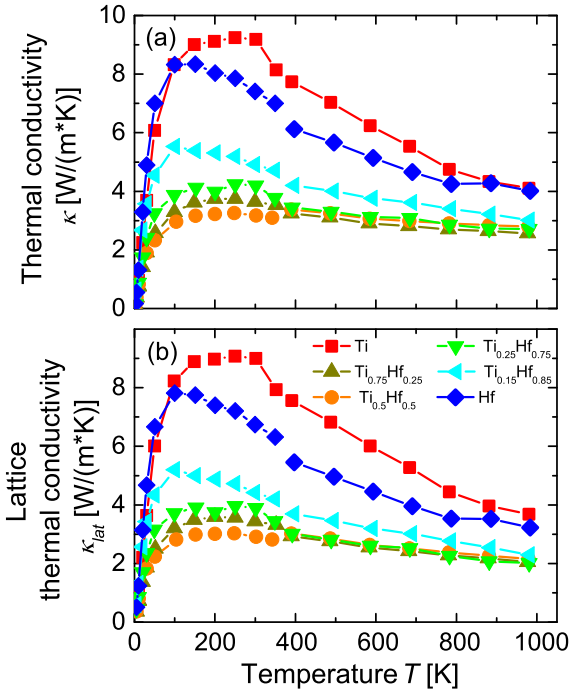

Fig. 4 (a) Thermal conductivity κ, and (b) lattice thermal conductivity κ_{lat} as functions of temperature for $Ti_{1-x}Hf_xCoSb_{0.8}Sn_{0.15}$ for the indicated ratios of Ti to Hf. Data up to 350 K were obtained from TTO PPMS measurements, high-temperature data were calculated from LFA measurements.

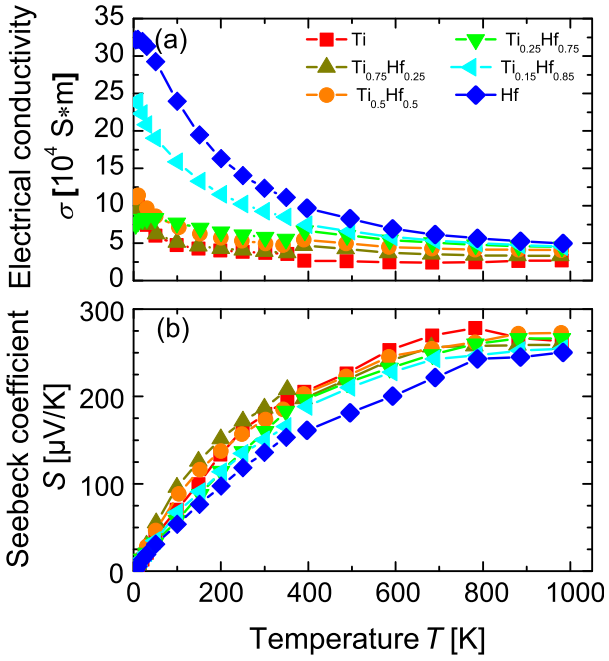

Fig. 5 (a) Electrical conductivity σ and (b) Seebeck coefficient S as functions of temperature for $Ti_{1-x}Hf_xCoSb_{0.85}Sn_{0.15}$ with the indicated ratio of Ti to Hf. Data up to 350 K were obtained from TTO PPMS measurements, high-temperature from LSR measurements.

of 50% and more. At 980 K, we obtained power factors between 2.93 $mWK^{-2}m^{-1}$ ($x = 0.15$) and 3.18 $mWK^{-2}m^{-1}$ ($x = 0.25$). These values correspond to a power factor enhancement of 89% with respect to that of $TiCoSb_{0.85}Sn_{0.15}$ (1.68 $mWK^{-2}m^{-1}$ at 980 K).

From Figure 6 we note that fine-tuning of the Ti–Hf ratio has a significant impact on the figure of merit ZT. By simply mixing Ti and Hf together in a 50% ratio, ZT shows a immediate improvement by 42% compared to the sample with only Hf. Since both samples exhibit similar power factors, this improvement is due to reduction in the lattice thermal conductivity by intrinsic phase separation. Adjustment of the ratio of Ti to Hf enhances ZT further. The selection of the optimal electronic properties in combination with the lowest thermal conductivity leads to the maximum figure of merit of $ZT \approx 1.2$ at 710°C for $Ti_{0.25}Hf_{0.75}CoSb_{0.85}Sn_{0.15}$. This value clearly exceeds the benchmark of $ZT \approx 1$ for device applications.[5] This result can be considered as very significant for bulk p-type half-Heuslers. When compared with the previous state-of-the-art material, e.g., $Ti_{0.12}Zr_{0.44}Hf_{0.44}CoSb_{0.8}Sn_{0.2}$[18] with $ZT = 0.98$ at 700°C, this value corresponds to an improvement of 19%. Considering only ingot samples prepared by a simple arc melting fabrication process as in reference[21], the enhancement of the figure of merit exceeds 125% by our combined approach of phase separation and carrier concentration adjustment.

4 Conclusions

Two concepts were successfully applied to improve the thermoelectric properties of the p-type TiCoSb system. Starting from $Ti_{0.5}Hf_{0.5}CoSb_{0.8}Sn_{0.2}$, it was shown that phase separation ($ZT = 0.9$ at 710°C[19]) affords thermoelectric properties that are similar to those obtained with nanostructuring approach involving ball milling.[17] In the second step, the optimization of the carrier concentration led to an improvement of about 25% as regards the figure of merit in $Ti_{0.5}Hf_{0.5}CoSb_{0.85}Sn_{0.15}$ ($ZT = 1.05$). Based on these two concepts a fine tuning of the Ti to Hf ratio for optimum phonon scattering in combination with optimum electronic properties, we achieved a maximum ZT of 1.2 at 710°C in $Ti_{0.25}Hf_{0.75}CoSb_{0.85}Sn_{0.15}$. When compared with the ZT value of the previous state-of-the-art p-type half-Heusler material, $Ti_{0.12}Zr_{0.44}Hf_{0.44}CoSb_{0.8}Sn_{0.2}$[18] with a $ZT \approx 1.0$ at 700°C, this value corresponds to an improvement of 20%. In conclusion, we realized a bulk p-type half-Heusler material with TE performance as good as the state-of-the art n-type $Ti_{0.5}Zr_{0.25}Hf_{0.25}NiSn_{0.998}Sb_{0.002}$ ($ZT = 1.2$ at 560 °C).[9] As both materials are compatible and perform well together in one TE module,[2] TE devices based on phase-separated half-Heusler compounds are very promising for applications in the mid-temperature range.

5 Acknowledgements

The authors gratefully acknowledge financial support by the DFG Priority Program 1386 Nanostructured Thermoelectric Materials under proposal BA 4171/2-2 and the thermoHEUSLER Project (Project No. 0327876D) of the German Federal Ministry of Eco-

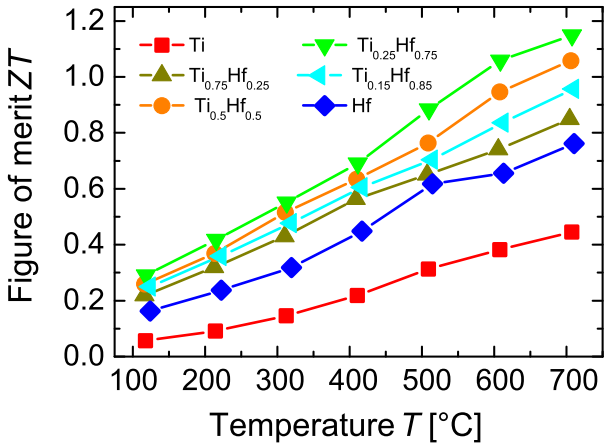

Fig. 6 Figure of merit ZT as a function of temperature for $Ti_{1-x}Hf_xCoSb_{0.8}Sn_{0.15}$ for the indicated ratios of Ti to Hf.

nomics and Technology (BMWi). We thank Sylvia Kostmann for specimen preparation for the microstructural examination, Monika Eckert and Petra Scheppan for SEM images and EDX measurements, and Dr. Walter Schnelle for characterization with the PPMS. We also thank the staff of the LNLS (Campinas) for support as well as Dean H. Barrett (LNLS, Campinas) for help with the XRD experiments. This work was further supported by the Brazilian Synchrotron Light Laboratory (LNLS) under proposals XPD - 17015 and by the DAAD (Project No. 57060637).

References

1 J.-W. G. Bos and R. A. Downie, J. Phys. Condens. Matter, 2014, **26**, 433201.
2 K. Bartholomé, B. Balke, D. Zuckermann, M. Köhne, M. Müller, K. Tarantik and J. König, J. Electron. Mater., 2014, **43**, 1775–1781.
3 T. Graf, C. Felser and S. S. P. Parkin, Prog. Solid State Chem., 2011, **39**, 1–50.
4 W. Xie, A. Weidenkaff, X. Tang, Q. Zhang, J. Poon and T. M. Tritt, Nanomaterials, 2012, **2**, 379–412.
5 S. Chen and Z. Ren, Mater. Today, 2013, **16**, 387–395.
6 J. Krez, J. Schmitt, G. J. Snyder, C. Felser, W. Hermes and M. Schwind, J. Mater. Chem. A, 2014, **2**, 13513–13518.
7 H. Geng and H. Zhang, J. Appl. Phys., 2014, **116**, 033708.
8 K. Galazka, S. Populoh, L. Sagarna, L. Karvonen, W. Xie, A. Beni, P. Schmutz, J. Hulliger and A. Weidenkaff, Phys. Status Solidi A, 2014, **211**, 1259–1266.
9 M. Schwall and B. Balke, Phys. Chem. Chem. Phys., 2013, **15**, 1868–1872.
10 R. A. Downie, D. MacLaren, R. I. Smith and J.-W. G. Bos, Chem. Commun., 2013, **49**, 4184–4186.
11 Y. Kimura, H. Ueno and Y. Mishima, J. Electron. Mater., 2009, **38**, 934–939.
12 M. Schwall, B. Balke and M. Köhne, Patent Application 20140127070 (May 08, 2014).
13 S. Sakurada and S. Hirono, US Patent Application US2005/0217715 A1 (October 06, 2005).
14 N. Shutoh, S. Sakurada, N. Kondo and N. Takezawa, US Patent Application US20050172994 A1 (August 11, 2005).
15 M. Köhne, T. Graf, H. J. Elmers and C. Felser, Patent Application 20130156636 (June 20, 2013).
16 J. Krez, B. Balke, C. Felser, W. Hermes and M. Schwind, arXiv:1502.01828 [cond-mat.mtrl-sci], 6 Feb 2015.
17 X. Yan, W. S. Liu, H. Wang, S. Chen, J. Shiomi, K. Esfarjani, H. Z. Wang, D. Z. Wang, G. Chen and Z. F. Ren, Energ. Environ. Sci., 2012, **5**, 7543–7548.
18 X. Yan, W. Liu, S. Chen, H. Wang, Q. Zhang, G. Chen and Z. F. Ren, Adv. Energy Mater., 2013, **3**, 1195–1200.
19 E. Rausch, B. Balke, S. Ouardi and C. Felser, Phys. Chem. Chem. Phys., 2014, **16**, 25258–62.
20 X. Yan, G. Joshi, W. Liu, Y. Lan, H. Wang, S. Lee, J. W. Simonson, S. J. Poon, T. M. Tritt, G. Chen and Z. F. Ren, Nano Lett., 2011, **11**, 556–60.
21 S. R. Culp, J. W. Simonson, S. J. Poon, V. Ponnambalam, J. Edwards and T. M. Tritt, Appl. Phys. Lett., 2008, **93**, 022105.
22 C.-C. Hsu, Y.-N. Liu and H.-K. Ma, J. Alloys Compd., 2014, **597**, 217–222.
23 E. Rausch, B. Balke, T. Deschauer, S. Ouardi and C. Felser, APL Mat., 2015, **3**, 041516.
24 F. F. Ferreira, E. Granado, W. Carvalho Jr, S. W. Kycia, D. Bruno and R. Droppa Jr, J. Synchrotron Radiat., 2006, **13**, 46–53.
25 B. Balke, S. Ouardi, T. Graf, J. Barth, C. G. F. Blum, G. H. Fecher, A. Shkabko, A. Weidenkaff and C. Felser, Solid State Commun., 2010, **150**, 529–532.
26 P. Sahoo, Y. Liu, J. P. A. Makongo, X.-L. Su, S. J. Kim, N. Takas, H. Chi, C. Uher, X. Pan and P. F. P. Poudeu, Nanoscale, 2013, **5**, 9419–9427.
27 H.-S. Kim, Z. M. Gibbs, Y. Tang, H. Wang and G. J. Snyder, APL Mat., 2015, **3**, 041506.

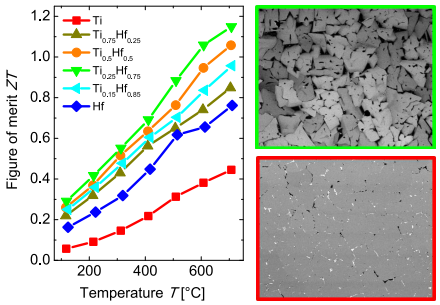

An efficiently designed microstructure leads to a record *ZT* value in *p*-type half-Heusler compounds.